PAPER

Check for updates

Construction of PtSe$_2$/Ge heterostructure-based short-wavelength infrared photodetector array for image sensing and optical communication applications†

Yu Lu,[a] Yue Wang,[a] Chenhao Xu,[a] Chao Xie,*[a,b] Wenbin Li,[a] Jie Ding,[a] Wanying Zhou,[a] Zipeng Qin,[a] Xinyi Shen[a] and Lin-Bao Luo [ID] *[a]

In this work, we present the construction of a multilayered PtSe$_2$/Ge heterostructure-based photodetector array comprising 1 × 10 device units operating in the short-wavelength infrared (SWIR) spectrum region. The as-fabricated heterostructures show an obvious photovoltaic effect, providing the devices with the ability to work as self-driven photodetectors. Upon 1550 nm illumination, a typical photodetector exhibits prominent photoresponse performance with the current on/off ratio, responsivity, external quantum efficiency and specific detectivity reaching 1.08×10^3, 766 mA W^{-1}, 61.3% and 1.1×10^{11} Jones, respectively. The device also has a fast response speed with rise/fall times of 54.9 μs/56.6 μs. Thanks to the respectable homogeneity in device performance, the photodetector array can reliably record an image of a "diode symbol" produced by SWIR irradiation. What is more, the photodetector is successfully integrated into a SWIR optical communication system serving as an optical receiver to transmit a text signal. The above results imply a huge possibility of the present heterostructure-based photodetector array for some optoelectronic purposes such as SWIR image sensing and optical communication applications.

Introduction

Light detection in the short-wavelength infrared (SWIR, typically 700–3000 nm) spectrum region has long garnered enormous research enthusiasm due to its wide military and civil applications, *e.g.*, night vision, optical communication, target detection, environmental monitoring, surveillance, remote sensing imaging, and so on.[1,2] High-performance SWIR photodetectors are pivotal components of many electronic and optoelectronic products such as laser rangefinder, night vision viewer, thermal imaging system, infrared digital camera and medical diagnostics apparatus.[3–5] Currently, the majority of the commercially available SWIR photodetectors are made from traditional inorganic semiconductors including crystalline Si, Si/Ge heterostructures and III–V semiconductor alloys (primarily InGaAs and its related heterostructures).[6,7] Nevertheless, the fabrication of these SWIR photodetectors normally requires high-quality epitaxially grown photoactive

materials, expensive high-vacuum instruments and complex multistep manufacturing procedures, which renders them uneconomical and also hampers their extensive applications. In recent years, there is great interest in exploring SWIR photodetectors based on novel functional materials with narrow bandgaps, *e.g.*, InAs nanowires (NWs),[8,9] PbS colloidal quantum dots (QDs)[10,11] and narrow bandgap organic semiconductors (OSCs).[12,13] These photodetectors are particularly suitable for some special uses requiring mechanical flexibility, large area or color adjustability.[14] Although some achievements have already been attained, the difficulties in device assembly of NW-based detectors and the slow response speed of QD- and OSC-based devices due to low charge carrier mobilities still limit their practical applications for many optoelectronic purposes.

As an alternative solution to the above circumstances, the study on SWIR photodetectors based on hybrid heterostructures combining graphene or other emerging two-dimensional (2D) layered materials with traditional narrow bandgap semiconductors, *e.g.*, GaAs and Ge, has recently attracted particular research interest.[15–18] In these heterostructures, the narrow bandgap semiconductor normally serves as the photoactive media to absorb incident SWIR illumination to produce electrons and holes, which are then separated at the heterostructure interface, and the 2D layered material typically acts

[a]School of Electronic Science and Applied Physics, Hefei University of Technology, Hefei, Anhui 230009, P. R. China. E-mail: chaoxie@ahu.edu.cn, luolb@hfut.edu.cn
[b]School of Electronics and Information Engineering, Anhui University, Hefei, Anhui 230601, P. R. China
†Electronic supplementary information (ESI) available: Fig. S1–S4. See DOI: 10.1039/d1nr00333j

as an active layer to transport photocarriers.[19–21] Due to simple device geometries and ease of manufacturing, the above heterostructure-based devices are very promising for developing low-cost high-performance SWIR photodetectors. For example, by transferring chemical vapor deposition (CVD)-prepared monolayer graphene atop a Ge wafer, our group has demonstrated a sensitive SWIR photodetector, which has a decent responsivity of 51.8 mA W^{-1} and a specific detectivity of 1.38×10^{10} Jones under 1550 nm illumination.[22] Benefiting from the pronounced light confinement effect, the responsivity of a graphene/Ge nanostructure array-based heterostructure modified with ITO nanoparticles could be improved by more than 3 times to ~185 mA W^{-1}.[23] Furthermore, by using a transparent ZnO top gate to modulate the barrier height of the heterostructure, Chang et al. has dramatically enhanced the responsivity to as high as ~750 mA W^{-1}, comparable to commercial Ge-based SWIR photodiodes.[24] In addition to graphene, other 2D layered materials, e.g., MoS_2, $MoTe_2$ and the newly explored group-10 transition metal dichalcogenides (TMDs), have also been employed for designing high-performance SWIR photodetectors.[25–27] Combining these 2D layered materials with diverse physical properties with Ge may bring about some novel functionalities. For instance, a SWIR photodetector composed of multilayered $PtSe_2$ transferred atop a Ge substrate was highly sensitive to 1550 nm irradiation, exhibiting a responsivity and specific detectivity of about 602 mA W^{-1} and 6.3×10^{11} Jones, respectively.[28] Very recently, Wu and colleagues reported the design of a SWIR photodetector based on a graphene/multilayered $PdSe_2$/Ge heterostructure, which possessed an outstanding photoresponse to SWIR illumination with an ultrahigh polarization sensitivity of about 112.2, enabling the preliminary realization of polarization optical imaging.[29] However, up to now, although the above SWIR photodetectors based on a single device unit have attained respectable photoresponse performance, the device integration has rarely been demonstrated, which requires intra-device isolation and crosstalk depressing between adjacent devices, and is of critical importance for developing complex optoelectronic systems towards practical applications.

Herein, we present a multilayered $PtSe_2$/Ge heterostructure-based SWIR photodetector array composed of 1×10 device units, which is fabricated by patterning the transferred $PtSe_2$ film atop a Ge substrate with the assistance of the traditional UV photolithography and reactive ion etching (RIE) techniques. Thanks to the pronounced photovoltaic behavior, the as-constructed heterostructures can operate as self-driven photodetectors with prominent photoresponse performance when subjected to 1550 nm irradiation. The important performance parameters such as current on/off ratio, responsivity, external quantum efficiency (EQE) and specific detectivity can reach 1.08×10^3, 766 mA W^{-1}, 61.3% and 1.1×10^{11} Jones, respectively, at zero bias. In addition, the response speed is calculated to be 54.9 and 56.6 μs for the rise and fall times. What is more, the photodetector array shows uniform photoresponse performance of all 10-device units, endowing it with the ability to function as a high-resolution SWIR optical image

sensor, which can reliably record an image of a "diode symbol". Furthermore, by acting as an optical receiver in a SWIR optical communication system to transmit a text signal, the present heterostructure-based photodetector also demonstrates a huge possibility for SWIR optical communication applications.

Experimental

Materials preparation and characterization

In this work, the multilayered $PtSe_2$ film was synthesized via a thermal-assisted selenization method, and the details are described in our previous studies.[28,31] The morphology of the as-obtained $PtSe_2$ was observed by SEM (Hitachi, SU8020). The topography was characterized by AFM (Benyuan Nanotech Com, CSPM-4000). The Raman spectrum of the sample was recorded on an HR Evolution (Horiba Jobin Yvon) Raman spectrometer equipped with a 532 nm laser.

Device fabrication and analysis

To fabricate the heterostructure-based photodetector array, an n-type Ge (resistivity: 0.1–6 Ω cm^{-1}) substrate covered with a ~60 nm Al_2O_3 insulating layer was used as the substrate. Prior to use, the substrate was ultrasonically cleaned in acetone, ethanol and deionized (DI) water for 15 minutes in sequence. First, a traditional UV photolithography and lift-off process was employed to define 1×10 exposed square windows with the size of 600×600 μm^2 on the substrate. Then the substrate was immersed in a hydrochloric acid solution (HCl : H_2O = 1 : 2) for 4 hours to etch away the Al_2O_3 layer within the exposed areas. After removing the photoresist in acetone, a multilayered $PtSe_2$ film was transferred atop the substrate through a polymethylmethacrylate (PMMA)-assisted transfer technique. Then, with the help of another UV photolithography and lift-off process, 1×10 photoresist protecting layers were defined atop the above exposed window areas. After that, the substrate was placed into a RIE chamber, where an oxygen RIE etching process was employed to etch away the exposed $PtSe_2$, rendering a 1×10 patterned $PtSe_2$ film array. Finally, the top Au electrode (~50 nm) was deposited on $PtSe_2$ via UV photolithography and electron beam deposition, and In–Ga alloy was attached to the rear side of the Ge substrate to serve as the bottom electrode.

The electrical measurement was carried out on a semiconductor analysis system (4200-SCS, Keithley Co. Ltd). Laser sources with varied wavelengths (THORLABS, M1300L3, M1550L3, M1650L3, and LR-ISP-2200-BG71680, laser LSR1550NL-1W-FC) were employed to perform the study of photoelectric properties. For response speed measurement, light irradiation with different modulating frequencies was produced by the laser diode driven by a signal generator (RGOL-DG5252), and the output electrical signal was recorded using a digital oscilloscope (Tektronix, DPO5104B). To perform optical communication application, a transimpedance amplifier (TLC2201-V2) was used to translate the current signal to

the voltage signal, and a microcontroller board (Arduino Uno) was employed to drive the laser diode and amplifier, as well as to perform the transformation between digital and analog signals.

Results and discussion

The multilayered PtSe₂/Ge heterostructure-based photo-detector array was constructed by patterning a transferred PtSe₂ film atop a Ge substrate with the aid of UV photolitho-graphy and oxygen RIE etching processes. The schematic diagram of the procedures for device fabrication is shown in Fig. 1a, and the details are provided in the "Experimental section". Fig. 1b displays a scanning electron microscopy (SEM) image of the PtSe₂ film transferred atop the Ge sub-strate, from which a large-area continuous film with good uni-formity could be observed. The film had a thickness of about 31 nm, as determined by the atomic force microscopy (AFM) image together with the height profile (Fig. S1†). Furthermore, the Raman spectrum in Fig. 1c indicated two distinct peaks situated at 177 cm⁻¹ and 203 cm⁻¹, which could be assigned to the E_g in-plane vibrational mode of Se atoms and A_{1g} out-of-plane vibration mode, respectively.[30] The results implied that a high-quality multilayered PtSe₂ film in a large-area was suc-cessfully prepared.

The electrical and optoelectrical characteristics of a repre-sentative PtSe₂/Ge heterostructure-based photodetector were first studied in darkness and under 1550 nm SWIR illumina-tion. As illustrated in Fig. 2a, the heterostructure displayed a distinct current rectifying effect with a decent rectification ratio of ∼430 at ±1.5 V. Interestingly, when illuminated with 1550 nm irradiation with an intensity of 701 mW cm⁻², we observed an apparent photovoltaic (PV) activity with a photo-voltage of ∼119 mV and a photocurrent of ∼135 μA, leading to
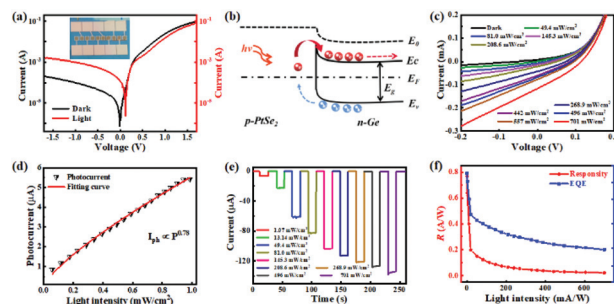
Fig. 2 (a) The I−V curves of a typical heterostructure-based photo-detector in darkness and under 1550 nm illumination. The inset shows the digital photography of the as-constructed photodetector array. (b) Energy band diagram of the PtSe₂/Ge heterostructure under light illumi-nation at zero bias. (c) The I−V curves of the device under 1550 nm illu-mination with different light intensities. (d) The photocurrent at zero bias as a function of incident light intensity. (e) The time-dependent photoresponse of the device upon 1550 nm illumination with different light intensities. (f) Responsivity and EQE as functions of incident light intensity.

a power conversion efficiency of ∼0.17%. Such a PV effect enabled the heterostructure to function as a self-driven photo-detector operating in the absence of an exterior power supply. To deeply understand the operational principle, the energy band diagram and related carrier transport process of the heterostructure were then plotted and analyzed. The work function of multilayered PtSe₂ with a semi-metallic feature was about ∼4.84 eV,[31,32] while the value was about ∼4.31 eV for n-Ge with the resistivity of 0.1–6 Ω cm⁻¹.[33] If the two com-ponents contact with each other, owing to the different work functions, electrons would diffuse from Ge to PtSe₂ and posi-tively charged empty states would then be left within Ge to form a depletion region until alignment of the Fermi levels. Consequently, as illustrated in Fig. 2b, the energy levels near the surface of Ge was bent upward, leading to the formation of a built-in electric field with the direction from Ge to PtSe₂ at the heterostructure interface. When under 1550 nm illumina-tion, photon absorption by Ge produced numerous electron–hole pairs. Those charge carriers generated within or in the vicinity of the depletion region were quickly separated towards opposite directions by the built-in electric field. The electrons crossed through the Ge substrate and were collected by the In–Ga electrode, whereas the holes transported through the PtSe₂ and arrived at the Au electrode, ultimately rendering the gene-ration of photocurrent at zero bias. Of note, when illuminated with SWIR illumination with the photon energy below the bandgap of Ge (∼0.67 eV), optical absorption could still take place within the PtSe₂ film as well.[34] In this case, according to the internal photoemission theory observed typically in Schottky junction photodiodes,[19,33] photoexcited carriers holding energy higher than the barrier height of the hetero-structure would surmount the barrier and be swept into the conduction band of the Ge. This process would give the gene-ration of photocurrent as well. Therefore, it was expected that our heterostructure-based photodetector could respond to the
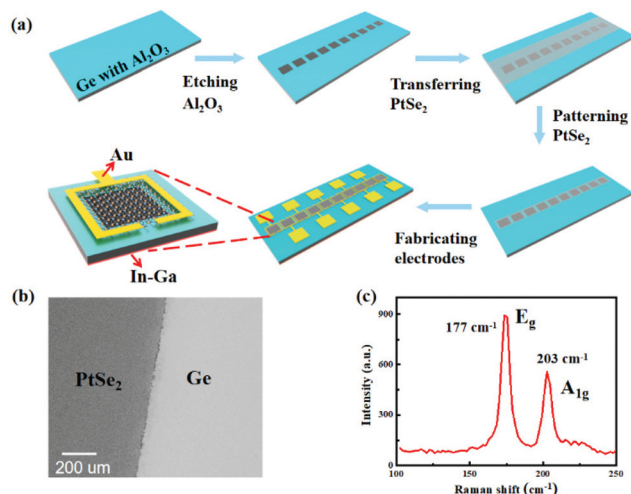
Fig. 1 (a) The schematic diagram of the fabrication procedures for the multilayered PtSe₂/Ge heterostructure-based photodetector array. (b) The SEM image and (c) Raman spectrum of the as-prepared PtSe₂.

SWIR illumination beyond the absorption limit of crystalline Ge (~1850 nm).

The photoresponse properties of the PtSe$_2$/Ge heterostructure depended significantly on the intensity of incident SWIR illumination. Fig. 2c depicts the current–voltage (I–V) curves upon 1550 nm illumination with varied intensities. Apparently, both the photovoltage and photocurrent increased gradually with increasing light intensity. Further analysis found that the photovoltage rose from ~18 mV to ~119 mV (Fig. S2a†) and the photocurrent increased from ~6 μA to ~135 μA (Fig. 2d), when the light intensity was changed from 1.07 mW cm^{-2} to 701 mW cm^{-2}. This phenomenon should be ascribed to the increased number of photocarriers under light illumination with an elevated intensity. In addition, the above dependence could be understood through linearity fitting of the photocurrent *versus* light intensity curve according to a generally used relationship: $I_{ph} = aP^b$, where I_{ph}, a, P, and b denote the net photocurrent, a constant related to the incident light wavelength, the light intensity and an empirical exponent associated with the recombination process of photocarriers, respectively.[35] As observed in Fig. 2d, fitting the curve rendered a non-ideal value of 0.78, signifying the presence of some recombination loss in our device.[36] Such a non-linear photoresponse was likely caused by the intensified carrier recombination rate due to the increased concentration of photocarriers at the high light intensity, as well as the existence of defect trap states between the Fermi level and conduction band edge.[37] Furthermore, as seen from Fig. 2e, the time-dependent photoresponse under light illumination with different intensities displayed the same evolution tendency. The sharp rise and fall edges also signified an efficient separation and collection of photocarriers in the heterostructure, as well as a fast response speed of the device.

To compare the photoresponse performance more quantitatively, some critical performance parameters, *i.e.*, responsivity (R), external quantum efficiency (EQE) and specific detectivity (D*), were evaluated according to the following formulae:[38]

$$R = \frac{I_{photo} - I_{dark}}{PS} = EQE\left(\frac{e\lambda}{hc}\right)G \qquad (1)$$

$$D^* = \frac{RS^{1/2}}{(2eI_{dark})^{1/2}} \qquad (2)$$

where I_{photo}, I_{dark}, P, S, e, λ, h, c and G represents the photocurrent, dark current, incident light intensity, effective device area, elementary charge, incident light wavelength, Planck constant, speed of light and photocurrent gain, respectively. Because of lacking an internal gain mechanism, the G should be unit in a PV-type photodiode.[39] Therefore, based on our experimental data and the above equations, the values of R, EQE and D^* were calculated to be ~766 mA W^{-1}, ~61.3% and ~1.1 × 10^{11} Jones, respectively, at 1550 nm illumination with a low light intensity of ~0.058 mW cm^{-2}. The large R value far exceeded that of graphene/Ge heterostructure-based detectors at zero bias (51.8–185 mA W^{-1}),[22,23] and was comparable to that of a graphene/Ge heterostructure-based detector at a large

gate bias (~750 mA W^{-1})[24] and group-10 TMDs/Ge heterostructure-based detectors composed of an individual device unit (530–691 mA W^{-1}).[27–29] Additionally, the dependence of R and EQE on the incident light intensity was also explored. As illustrated in Fig. 2f, both values declined monotonously with the increase in light intensity, which again confirmed the existence of recombination loss in this light intensity regime.

Furthermore, we studied the photoresponse of the heterostructure-based photodetector under incident light irradiation with different wavelengths at a constant optical intensity (~1.0 mW cm^{-2}). As illustrated in Fig. S2b,† the detector exhibited a distinct photoresponse over a wide wavelength spectrum from 400 to 2200 nm, suggesting a broadband photodetection characteristic. The photoresponse first rose gradually when the light wavelength was changed from the visible to SWIR region and then declined when the light wavelength exceeded 1550 nm, with the maximum photoresponse situated at around 1550 nm. To understand the light wavelength-dependent response properties more deeply, the time-dependent photoresponse to periodically switched light irradiation with the wavelengths of 1300, 1550, 1650 and 2200 nm was studied as well. As depicted in Fig. S2c–f,† the photodetector showed a fast and reliable photoresponse with good repeatability to all illumination. The evolution tendency of photocurrent with light wavelength was in accordance with the observation shown in Fig. S2b.† In addition, the sub-bandgap photoresponse at 2200 nm could be ascribed to the internal photoemission process in the PtSe$_2$/Ge heterostructure, as we discussed in the above energy band diagram analysis section.

The uniformity of photoresponse performance is vital to the photodetector array for its application in practical uses. Therefore, we further probed the performance uniformity by separately characterizing and comparing the optoelectrical properties of all 10-device units. Fig. 3a illustrates the dark currents and photocurrents upon homogeneous 1550 nm SWIR
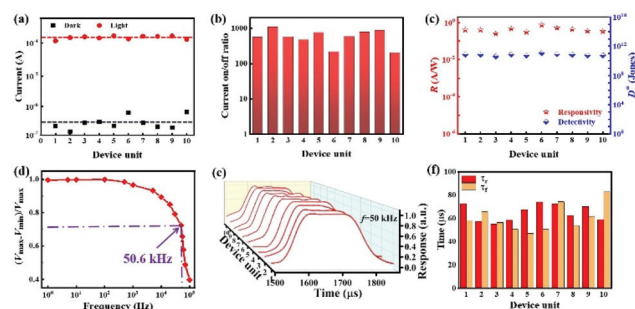

Fig. 3 (a) Current in darkness and under 1550 nm SWIR illumination, (b) current on/off ratio, and (c) R and EQE for all the 10-device units. The dashed lines in (a) denote the mean values for dark current (black) and photocurrent (red). (d) Relative balance ($V_{max} - V_{min}$)/V_{max} as a function of the light modulating frequency, showing a 3 dB cutoff frequency of ~50.6 kHz. (e) Individual magnified photoresponse of the 10-device units for determining the rise/fall times. (f) The rise and fall times of the 10-device units.

illumination with an intensity of ~701 mW cm^{-2}, extracted from time-dependent photoresponses at zero bias. Clearly, all device units could work properly. Careful analysis found that the dark currents were in the region of 0.13–0.65 µA with a mean value of 0.31 µA, and the photocurrents were in the range of 0.13–0.16 mA with a mean value of 0.15 mA. The current on/off ratios of these devices were extracted and summarized as well, as shown in Fig. 3b. It was observed that the majority of device units had a current on/off ratio between 5.5 × 10^2 and 8.6 × 10^2, and the average value was around ~6.9 × 10^2. Fig. 3c further displays the values of R and D^* of all device units (at a light intensity of ~0.058 mW cm^{-2}), indicating a narrow distribution of both parameters. The average values of R and D^* were ~419 mA W^{-1} and ~6.63 × 10^{10} Jones, respectively. In addition to the above parameters, the response speed, a key figure-of merit related to the ability of a photodetector to respond to fast-varying optical signals, was also explored for all device units. Fig. S3† depicts the photoresponse of a typical device to the pulsed SWIR illumination with different modulating frequencies of 0.01, 1, 5, 10, 50 and 100 kHz. Significantly, the photodetector could show stable and repeatable optical switching properties upon all illuminating conditions. At a high modulation frequency of 100 kHz, although suffering from some degradation, the present detector was still able to clearly distinguish the low and high photovoltage status, implying a fast response speed. In addition, by analyzing the relationship between the relative balance $(V_{max} - V_{min})/V_{max}$ and the modulating frequency (Fig. 3d), the 3 dB bandwidth, described as the frequency at which the photoresponse drops to 0.707 of the maximum value, was deduced to be ~50.6 kHz. Furthermore, to extract the rise and fall times (τ_r and τ_f), individual magnified response curves of all device units at the modulating frequency of 50 kHz were summarized, which showed a similar evolutionary behavior (Fig. 3e). As illustrated in Fig. 3f, most of the device units exhibited a short τ_r and τ_f with the values below 70 µs, suggesting that they had fast response speeds. The mean values for τ_r and τ_f were estimated to be 65 µs and 60.1 µs, respectively. The above results signified that our photodetector array had good homogeneity in SWIR photoresponse performance, and therefore would be very promising for integrated optoelectronic applications.

The good uniformity of the photodetector array also enables it to provide a higher output signal to meet more practical applications by parallel connection of the device units (Fig. S4a†). Fig. S4b† depicts the I–V curves of the photodetector array connected in parallel with different unit numbers under 1550 nm irradiation with an intensity of ~16 mW cm^{-2}. Clearly, the photocurrent increased gradually with an increasing unit number, while the photovoltage keeps nearly identical. Specifically, the value of photocurrent at zero bias increased from 0.018, 0.021, 0.027, 0.048 to 0.051 mA, when the unit number changes from 1, 2, 4, 8 to 10.

To verify the above conjecture, the functionality of the photodetector array for SWIR image sensing was further explored. Fig. 4a schematically shows the setup for measurement. A uniform 1550 nm SWIR light irradiation was
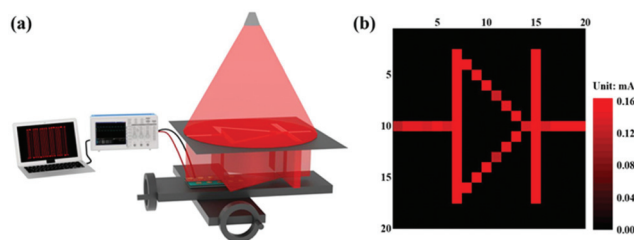
Fig. 4 (a) The schematic diagram of the setup for the SWIR light imaging. (b) The 2D current map of the photodetector array, showing the ability to record the image of a "diode symbol".

employed to illuminate upon the photodetector array fixed to a stepper motor, between which a lab-made shadow mask with a "diode symbol" hollow pattern was placed. Thus, only light illumination within the hollow regime of the mask could shine on the photodetector array. The currents of the 10-device units were first recorded, and then the stepper motor drove the detector array to progressively move vertically or horizontally towards the position of adjacent pixels to repeat the recording of current values. After measurement of all 20 × 20 pixels, the recorded currents were incorporated into a 2D current map. As shown in Fig. 4b, the profile of the "diode symbol" could be clearly identified with a respectable spatial resolution, implying the successful application of the present photodetectors array in SWIR light image sensing.

Finally, benefiting from the fast response speed, our heterostructure-based photodetector could be applied in a SWIR optical communication system working as a light receiver. Different from optical fiber communication that focuses SWIR illumination into a thin optical fiber, the SWIR optical communication was based on SWIR light propagating divergently in free space.[40,41] This wireless communication technique that could transmit information was also popularly known as "LIFI",[42] and had features of high security, high speed, low power consumption, immunity of electromagnetic interference, and capability of reducing the burden on the network.[40,43] The schematic diagram of the SWIR optical communication system is shown in Fig. 5, where a 1050 nm LED with an intensity of ~1.2 mW cm^{-2} was used as the light source and placed ~3 cm away from the photodetector. The digital photograph of our prototype system is shown in Fig. S5.† Data flow (digital signal) sent by a computer corresponded to a row of binary codes according to the criterion of ASCII, and was transferred into high- and low-voltage levels (analog signal, 1 and 0 corresponded to high- and low-voltage level, respectively) with the help of a driver. The voltage levels were employed to power a SWIR LED to generate modulated light illumination, which shinned upon the heterostructure-based photodetector to produce high- and low-level currents. The currents with different levels were first amplified by using a low noise current to voltage preamplifier, and then the voltage signals were input into another driver, where they were transferred into data flow. The data were ultimately collected by another computer to complete the information trans-
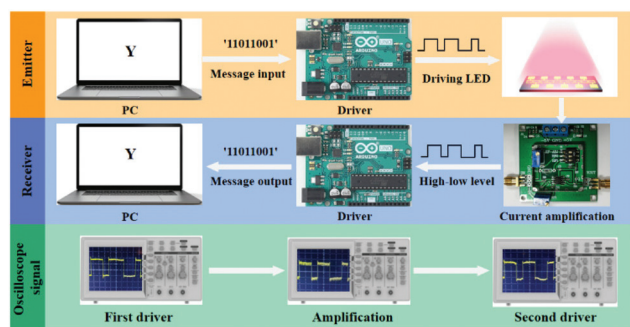
Fig. 5 The schematic diagram of the setup for the SWIR optical communication system and the waveforms of voltage signals collected by oscilloscopes from the output terminal of the first driver (top), the pre-amplifier (middle) and an additional pin of the second driver (bottom), respectively.

mission process. Fig. 5 also illustrates the waveforms of "11011001" voltage signals corresponding to a "Y" character collected by oscilloscopes from the output terminal of the first driver, the preamplifier and an additional pin of the second driver, at a transmit speed of 30 ms per bit (3.7 Byte per s), respectively. Apparently, the initial electrical signals could be well kept after transmission across the apparatus, indicating that the present photodetector was successfully used in the SWIR optical communication system to transmit information. The transmission of a text of "Hefei University of Technology" *via* our system was demonstrated in the videos in the ESI.† Of note, given the fast response speed of our device (∼70 μs), the present SWIR optical communication system was expected to work at a transmit speed as fast as ∼70 μs per bit (∼1.59 Kbyte per s). In addition, parallel transmission of multiple information was also realizable with our photodetectors array through additional configuration of the SWIR optical communication system.

Conclusions

In summary, a multilayered $PtSe_2$/Ge heterostructure-based 1 × 10 photodetector array working in the SWIR spectrum regime had been demonstrated. These heterostructures could operate as self-driven photodetectors originating from the pronounced PV effect. Photoresponse analysis revealed excellent photoresponse performance as well as decent homogeneity between device units. With 1550 nm illumination, the current on/off ratio, responsivity, EQE and specific detectivity had reached $1.08 × 10^3$, 766 mA W^{-1}, 61.3% and $1.1 × 10^{11}$ Jones, respectively, at zero bias. By reliably recording an image of a "diode symbol" projected by the SWIR illumination, the photodetectors array presented the ability of serving as a SWIR light image sensor. In addition, owing to the fast response speed, our photodetector could also be applied in a SWIR optical communication system serving as a light receiver, exhibiting the capability to transmit text information. It is believed that the present heterostructure-based photodetector array will find

important applications in future integrated SWIR optoelectronic systems.

Author contributions

L. L. and C. X. conceived the experiments. Y. L. fabricated the device. Y. W. and C. X. assisted with device fabrication and characterization. W. L., J. D., W. Z., Z. Q. and X. S. designed the circuits of optical communication. The manuscript was written by Y. L. and discussed by all authors.

Conflicts of interest

There are no conflicts to declare.

Acknowledgements

References

1 G. Konstantatos, I. Howard, A. Fischer, S. Hoogland, J. Clifford, E. Klem, L. Levina and E. H. Sargent, *Nature*, 2006, **442**, 180–183.

2 C. L. Tan and H. Mohseni, *Nanophotonics*, 2018, **7**, 169–197.

3 P. Martyniuk, J. Antoszewski, M. Martyniuk, L. Faraone and A. Rogalski, *Appl. Phys. Rev.*, 2014, **1**, 041102.

4 J. Li, L. Niu, Z. Zheng and F. Yan, *Adv. Mater.*, 2014, **26**, 5239–5273.

5 G. Rao, X. Wang, Y. Wang, P. Wangyang, C. Yan, J. Chu, L. Xue, C. Gong, J. Huang, J. Xiong and Y. Li, *InfoMat*, 2019, **1**, 272–288.

6 H. C. Ko, M. P. Stoykovich, J. Song, V. Malyarchuk, W. M. Choi, C. J. Yu, J. B. Geddes 3rd, J. Xiao, S. Wang, Y. Huang and J. A. Rogers, *Nature*, 2008, **454**, 748–753.

7 C. Xie and F. Yan, *Small*, 2017, **13**, 1701822.

8 J. Miao, W. Hu, N. Guo, Z. Lu, X. Zou, L. Liao, S. Shi, P. Chen, Z. Fan, J. C. Ho, T.-X. Li, X. S. Chen and W. Lu, *ACS Nano*, 2014, **8**, 3628–3635.

9 R. R. LaPierre, M. Robson, K. M. Azizur-Rahman and P. Kuyanov, *J. Phys. D: Appl. Phys.*, 2017, **50**, 123001.

10 T. Rauch, M. Böberl, S. F. Tedde, J. Fürst, M. V. Kovalenko, G. Hesser, U. Lemmer, W. Heiss and O. Hayden, *Nat. Photonics*, 2009, **3**, 332–336.

11 Z. Sun, Z. Liu, J. Li, G. Tai, S. P. Lau and F. Yan, *Adv. Mater.*, 2012, **24**, 5878–5883.

12 Q. Li, Y. Guo and Y. Liu, *Chem. Mater.*, 2019, **31**, 6359–6379.

13 X. Liu, Y. Lin, Y. Liao, J. Wu and Y. Zheng, *J. Mater. Chem. C*, 2018, **6**, 3499–3513.

14 F. P. García de Arguer, A. Armin, P. Meredith and E. H. Sargent, *Nat. Rev. Mater.*, 2017, **2**, 16100.

15 L. B. Luo, J. J. Chen, M. Z. Wang, H. Hu, C. Y. Wu, Q. Li, L. Wang, J. A. Huang and F. X. Liang, *Adv. Funct. Mater.*, 2014, **24**, 2794–2800.

16 J. Wu, Z. Yang, C. Qiu, Y. Zhang, Z. Wu, J. Yang, Y. Lu, J. Li, D. Yang, R. Hao, E. Li, G. Yu and S. Lin, *Nanoscale*, 2018, **10**, 8023–8030.

17 M. Zhao, Z. Xue, W. Zhu, G. Wang, S. Tang, Z. Liu, Q. Guo, D. Chen, P. K. Chu, G. Ding and Z. Di, *ACS Appl. Mater. Interfaces*, 2020, **12**, 15606–15614.

18 L. Pi, L. Li, K. Liu, Q. Zhang, H. Li and T. Zhai, *Adv. Funct. Mater.*, 2019, **29**, 1904932.

19 C. Xie, Y. Wang, Z. X. Zhang, D. Wang and L. B. Luo, *Nano Today*, 2018, **19**, 41–83.

20 J. Yao and G. Yang, *Nanoscale*, 2020, **12**, 454–476.

21 M. Long, P. Wang, H. Fang and W. Hu, *Adv. Funct. Mater.*, 2019, **29**, 1803807.

22 L.-H. Zeng, M.-Z. Wang, H. Hu, B. Nie, Y.-Q. Yu, C.-Y. Wu, L. Wang, J.-G. Hu, C. Xie, F.-X. Liang and L.-B. Luo, *ACS Appl. Mater. Interfaces*, 2013, **5**, 9362–9366.

23 R. Lu, C. W. Ge, Y. F. Zou, K. Zheng, D. D. Wang, T. F. Zhang and L. B. Luo, *Laser Photonics Rev.*, 2016, **10**, 595–602.

24 K. E. Chang, C. Kim, T. J. Yoo, M. G. Kwon, S. Heo, S. Kim, Y. Hyun, J. I. Yoo, H. C. Ko and B. H. Lee, *Adv. Electron. Mater.*, 2019, **5**, 1800957.

25 R. D. Mahyavanshi, G. Kalita, A. Ranade, P. Desai, M. Kondo, T. Dewa and M. Tanemura, *IEEE Trans. Electron Devices*, 2018, **65**, 4434–4440.

26 W. Chen, R. Liang, S. Zhang, Y. Liu, W. Cheng, C. Sun and J. Xu, *Nano Res.*, 2020, **13**, 127–132.

27 L. Luo, D. Wang, C. Xie, J. Hu, X. Zhao and F. Liang, *Adv. Funct. Mater.*, 2019, **29**, 1900849.

28 L. Wang, J. J. Li, Q. Fan, Z. F. Huang, Y. C. Lu, C. Xie, C. Y. Wu and L. B. Luo, *J. Mater. Chem. C*, 2019, **7**, 5019–5027.

29 D. Wu, J. Guo, J. Du, C. Xia, L. Zeng, Y. Tian, Z. Shi, Y. Tian, X. J. Li, Y. H. Tsang and J. Jie, *ACS Nano*, 2019, **13**, 9907–9917.

30 Z. X. Zhang, L. H. Zeng, X. W. Tong, Y. Gao, C. Xie, Y. H. Tsang, L. B. Luo and Y. C. Wu, *J. Phys. Chem. Lett.*, 2018, **9**, 1185–1194.

31 L. H. Zeng, S. H. Lin, Z. J. Li, Z. X. Zhang, T. F. Zhang, C. Xie, C. H. Mak, Y. Chai, S. P. Lau, L. B. Luo and Y. H. Tsang, *Adv. Funct. Mater.*, 2018, **28**, 1705970.

32 X. Yu, P. Yu, D. Wu, B. Singh, Q. Zeng, H. Lin, W. Zhou, J. Lin, K. Suenaga, Z. Liu and Q. J. Wang, *Nat. Commun.*, 2018, **9**, 1545.

33 S. M. Sze and K. K. Ng, *Phys. Semicond. Devices*, 2007.

34 Y. Zhao, J. Qiao, Z. Yu, P. Yu, K. Xu, S. P. Lau, W. Zhou, Z. Liu, X. Wang, W. Ji and Y. Chai, *Adv. Mater.*, 2017, **29**, 1604230.

35 D. Wu, C. Jia, F. Shi, L. Zeng, P. Lin, L. Dong, Z. Shi, Y. Tian, X. Li and J. Jie, *J. Mater. Chem. A*, 2020, **8**, 3632–3642.

36 X. Li, M. Zhu, M. Du, Z. Lv, L. Zhang, Y. Li, Y. Yang, T. Yang, X. Li, K. Wang, H. Zhu and Y. Fang, *Small*, 2016, **12**, 595–601.

37 L. Wang, J. Jie, Z. Shao, Q. Zhang, X. Zhang, Y. Wang, Z. Sun and S. T. Lee, *Adv. Funct. Mater.*, 2015, **25**, 2910–2919.

38 J. D. Yao, Z. Q. Zheng and G. W. Yang, *Prog. Mater. Sci.*, 2019, **106**, 100573.

39 C. Xie, C. Liu, H. Loi and F. Yan, *Adv. Funct. Mater.*, 2020, **30**, 1903907.

40 C. Bao, J. Yang, S. Bai, W. Xu, Z. Yan, Q. Xu, J. Liu, W. Zhang and F. Gao, *Adv. Mater.*, 2018, **30**, 1803422.

41 C. Li, J. Lu, Y. Zhao, L. Sun, G. Wang, Y. Ma, S. Zhang, J. Zhou, L. Shen and W. Huang, *Small*, 2019, **15**, 1903599.

42 Q. Shan, C. Wei, Y. Jiang, J. Song, Y. Zou, L. Xu, T. Fang, T. Wang, Y. Dong, J. Liu, B. Han, F. Zhang, J. Chen, Y. Wang and H. Zeng, *Light: Sci. Appl.*, 2020, **9**, 163.

43 Z. Ma, Y. Zhang, T. Li, X. Tang, H. Zhao, J. Li, C. Ma and J. Yao, *Appl. Phys. A*, 2020, **126**, 869.